Measuring the multifunctional properties of MoS_2 across the amorphous-crystalline transition using colorimetric sensing

Jose L. Ocana-Pujol [1,*] Rebecca A. Gallivan [1] Ramón Camilo Domínguez Ordóñez [1] Nikolaus Porenta [1] Arnold Müller [2] Christof Vockenhuber,[2] Ralph Spolenak,[1] and Henning Galinski [1,†]

[1]*Laboratory for Nanometallurgy, ETH Zurich, 8093 Zürich, Switzerland*

[2]*Laboratory of Ion Beam Physics, ETH Zurich, 8093 Zürich, Switzerland*

(Received 14 May 2024; revised 28 June 2024; accepted 8 July 2024; published 5 September 2024)

Molybdenum disulfide (MoS_2) is a next-generation semiconductor and is frequently integrated into emergent optoelectronic technologies based on two-dimensional materials. Here, we present a method that provides direct optical feedback on the thickness and crystallinity of sputter-deposited MoS_2 down to the few-layer regime. This colorimetric sensing enables tracking the material's functional properties, such as excitonic response, sheet resistance, and hardness across the amorphous-crystalline transition. To illustrate the potential of such feedback-controlled fabrication, we realized MoS_2-based hyperbolic metamaterials (HMMs) with controllable optical topological transitions and hardness.

DOI: 10.1103/PhysRevB.110.115303

I. INTRODUCTION

Semiconductors are essential building blocks of the electronic devices that critically shape our daily lives [1]. However, the drive for device miniaturization faces challenges as we approach the fundamental physical limits of today's semiconductor technologies [2]. In this context, molybdenum disulfide (MoS_2), a transition metal chalcogenide (TMC), has emerged as a potential next-generation semiconductor. Unlike other TMCs, MoS_2 is composed of relatively abundant and relatively innoxious elements [3]. It also has a long history of being used in industry due to its catalytic [4,5] and mechanical properties [6,7]. These properties stem from the material's peculiar layered crystal structure, in which each layer consists of a molybdenum sheet sandwiched between two sheets of sulfur atoms. While in the plane these layers form a covalently bonded hexagonal lattice, they are only held together by weak van der Waals forces on the interlayer level [8].

As a consequence of weak interlayer bonding, single- to few-layer MoS_2 is readily produced by top-down approaches such as mechanical or chemical exfoliation. Similar to graphene, the electronic properties of MoS_2 change dramatically when the crystal is reduced to a single layer [9]. While bulk crystals have an indirect band gap (1.23 eV) requiring phonon interaction for bound electron-hole pair (exciton) formation, in the monolayer limit, MoS_2 exhibits a direct band gap (1.89 eV), featuring strong excitonic transitions [10]. Its tunable electronic properties make MoS_2 a promising material for various classical semiconductor applications such as transistors [11], photodetection [12], light-emitting diodes [13], solar cells [14], and emergent optoelectronic applications such logical gates based in spin- and valleytronics [15–17].

Despite the tempting prospects of MoS_2 as a next-generation semiconductor, the integration of MoS_2 into standard semiconductor fabrication processes remains a significant challenge. Although developments in top-down approaches such as exfoliation have proven capable of overcoming initial drawbacks in coverage and scalability, these techniques remain mainly limited to monolayer systems [18,19]. Similarly, bottom-up approaches such as chemical vapor deposition (CVD) require high annealing temperatures ($T > 1000$ K), limiting the choice of substrate materials on which MoS_2 can be grown [19,20]. All the mentioned techniques can only produce crystalline MoS_2 (c-MoS_2), leaving the properties of amorphous MoS_2 (a-MoS_2) not fully explored [21,22]. Notably, a-MoS_2 shows superior optical broadband absorbance [23] and hydrogen evolution reaction activities compared to c-MoS_2, making it more suitable for applications such as photodetectors and hydrogen catalysis [23,24].

To address these challenges, magnetron sputtering, which is a bottom-up fabrication technique well aligned with standard semiconductor fabrication processes, has been considered as an alternative route to fabricate MoS_2. Sputtering enables the production of both amorphous and crystalline MoS_2 with thicknesses ranging from one monolayer to more than one micrometer [25,26] on all vacuum-compatible substrates. Still, common drawbacks of sputtering are the high kinetic energy upon arrival, which is typical of the sputtering process, leading to a limited degree of epitaxy and an increase in defects in the material. Hence, to establish a fabrication procedure for sputtered MoS_2 with a high uniformity and controllable number of layers, it is imperative to develop tools that enable effective monitoring of the thickness, crystal structure, and uniformity postdeposition. In this work, we design a low-footprint thermochromic sensor to assist in the controlled deposition of amorphous and crystalline MoS_2 by magnetron sputtering.

*Contact author: joseo@ethz.ch

†Contact author: henningg@ethz.ch; http://met.mat.ethz.ch

The sensor relies on an asymmetric Fabry-Pérot-type resonator [27] that utilizes the optical losses in MoS_2 [28] to optically detect changes in thickness and crystal structure down to a monolayer. This in-place monitoring enables us to study the chemical and functional properties of MoS_2, such as exciton formation, hardness, and sheet resistance, across the amorphous-crystalline phase transition. We highlight the advantage of direct optical feedback within the fabrication process by realizing a MoS_2-based hyperbolic metamaterial and analyzing its functional properties.

II. SAMPLE PREPARATION AND EXPERIMENTAL DETAILS

The materials in this work were deposited using magnetron sputtering (*PVD Products Inc*). Molybdenum disulfide (99% *MaTecK GmbH*) was sputtered by radio frequency (RF) sputtering ($P_{RF} = 75$ mW), while zirconium nitride was deposited by reactive sputtering using a zirconium target (99.5% *MaTecK GmbH*) and constant nitrogen flow (3 sscm). The samples were annealed for 2 h in a vacuum at 1×10^{-9} mbar in a *Createc* rapid-thermal annealing (RTA) setup. Annealing under UHV conditions supresses reactions with water and oxygen and leads to desorption of physisorbed impurities [29]. The heating rate was kept at 5 K/min and no active cooling was used.

The refractive index of MoS_2 and ZrN was measured by Variable Angle Spectroscopic Ellipsometry (VASE) with a *J. A. Woollam* M-2000 system. A comparison between the experimental n and k values of magnetron sputtered MoS_2 and ZrO_xN_y with data from the corresponding literature is shown in Fig. S3 in Ref. [30]. M-2000 was also used to measure the angular and polarization-dependent reflectance spectra [Fig. 4(d)]. The reflectance spectra at near-normal incidence were measured using a fiber-coupled reflectometer (OceanOptics). Transfer Matrix (TM) calculations were performed on – *Wolfram Mathematica*. Photoluminescence measurements were performed on a Horiba microscope (LabRAM HR Evolution UV-VIS-NIR). A 532 nm Nd: Yag laser was used at a nominal power of 1.5 W and focused onto the samples with a Nikon PlanFluor 10x objective. The incident power was controlled through the filter wheel setting set at 10% after observing no shift in the optical response below that threshold. The integration time was kept constant to 45 s.

X-ray diffraction (XRD) measurements were performed using an (X'Pert MRD, Panalytical, Netherlands) equipped with a 0.27° parallel plate collimator. Cu $K_{\alpha 1}$ ($\lambda = 1.540598$ Å) radiation generated at 40 kV/45 mA was used. RBS measurements were performed with a 2 MeV ^{4}He beam and a Si PIN diode detector under 168° scattering angle. The results were fitted using RUMP. The Raman measurements were performed on a Witec Microscope CRM 200 with a 532 nm excitation. All measurements were performed in backscattering mode with an long pass edge filter filter (532 nm). A 20x objective with a numerical aperture of 0.4 was used. We refer to Ref. [30] for the details on the peak deconvolution (Table S3). The integration time was kept constant at 30 s.

The sheet resistance was measured using a linear four-point probe head with tungsten electrodes and a Keysight B2962A power supply. The current-voltage curves were measured in the Ohmic region, varying from nA to mA.

An iNano nanoindenter (*Nanomechanics, Inc.*) with an InForce50 actuator under a quasistatic strain rate of 0.1 s^{-1} using a diamond Berkovich indenter tip (*Synton-MDP*) was used for the indentation experiments. All MoS_2 thin film samples were indented to a depth of 20 nm in a 10×10 array. The load-displacement curves were inspected for artefacts and punch-through of the films, as indicated by a discrete shift in loading slope to identify successful indentation experiments. To appropriately account for the bluntness of our indentation tip at such small indentation depths, a spherical approximation with a 50 nm radius of curvature was made for the contact area. The MoS_2-ZrN multilayers were indented to a load of 1 mN in a 10×10 array to allow the penetration of multiple layers for all samples. The ZrN multilayers were indented in a 10×10 array to a load of 1 mN in four regions of the sample, leading to an average indentation depth of 47 nm. All hardness measurements are reported at the maximum indentation depth.

III. RESULTS AND DISCUSSION

A. Monitoring the bottom-up fabrication of MoS_2

To identify the operational regime of the thermochromic sensor, a-MoS_2 of varying thickness δ was deposited on zirconium nitride (ZrN) by RF magnetron sputtering. In a second step, crystallization is achieved by annealing at 750 K for two hours in ultrahigh vacuum (UHV), as illustrated in Fig. 1(a). Here, ZrN acts as a metallic back-reflector of the asymmetric cavity. ZrN was specifically selected as it guarantees high chemical stability in a sulfur-rich environment. We refer to Ref. [30] (Fig. S1) for a more detailed discussion on the selection of a metallic backreflector.

Figure 1(b) shows optical micrographs of amorphous and crystalline MoS_2 directly deposited on ZrN-coated Si wafers. In both states, we observe the formation of vivid structural colors spanning from yellow to green, depending on the thickness. This change in coloration is also seen in the reflectance spectra obtained by near-normal incidence reflectometry shown in Figs. 1(c) and 1(d). Similar to coinage metals, such as Ag, the spectra exhibit a characteristic absorption edge. The reflectance minimum observed in the spectra linearly red-shifts on average by 6.4 ± 0.5 nm (Fig. S2) due to an increase in thickness δ. The experimentally measured spectra are in good agreement with calculated spectra based on transfer matrix calculations [31,32] [Figs. 1(c) and 1(d)]. Refractive indexes were determined using ellipsometry (Fig. S3 [30]).

Upon crystallization, both the optical properties and structural coloration of the sputtered MoS_2 films change [Figs. 1(b)–1(e)]. The observed strong thermochromic response is due to the high absorption in the asymmetric optical cavity. The spectral position of the absorbing state (i.e., minimal reflectance) redshifts on average by 45 ± 25 nm for a given thickness δ due to an increase in refractive index upon crystallization (see also Fig. S3). Due to the high optical loss, the partially reflected waves are complex and the condition for destructive interference depends critically on the extinction coefficient k and the film thickness δ [33].

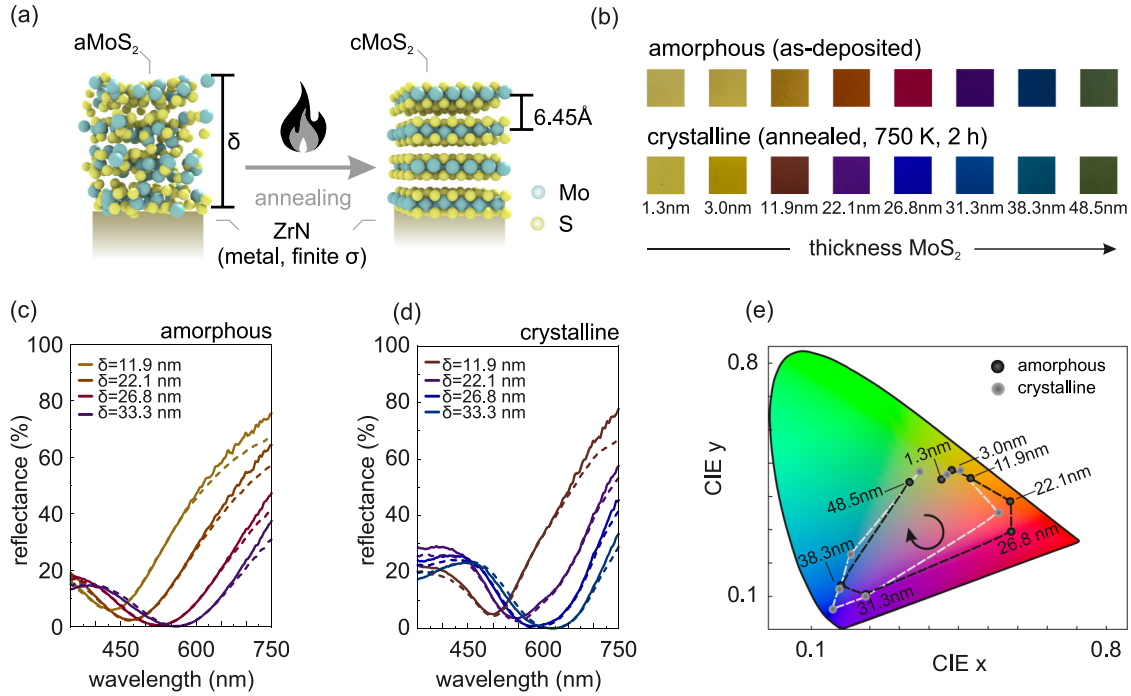

FIG. 1. (a) Schematic illustration of the thermochromic sensor in the amorphous and crystalline states. ZrN acts as an inert metallic backreflector and MoS_2 is the cavity medium. (b) Photographs of MoS_2 on top of ZrN-coated Si wafers ranging from two layers of MoS_2 to bulk MoS_2 before (top) and after annealing (bottom). The indicated thickness δ was measured by RBS. [(c) and (d)] Normal incidence reflectance spectra of MoS_2 on top of ZrN before and after annealing. Dashed lines correspond to TM calculations. (e) CIE 1931 color map showing the colors achieved in the samples in (b). The dark symbols indicate the colors of the amorphous samples, while the grey symbols indicate the colors of the crystalline samples.

While the thermochromic response can be identified by eye in the 11.9–38.3 nm thickness range, all configurations exhibit a measurable change in color as shown in the CIE color plot [Fig. 1(e)]. For both parameters, namely thickness and crystallinity, the sensor response spans the full gamut of structural colors, where each color corresponds to a unique experimental state. This direct correlation validates that the chosen thermochromic sensor configuration is well suited to act as a robust feedback mechanism in a thickness regime between 1.3–48.5 nm (2–80 MoS_2 layers). In the analyzed thickness regime, the attenuation and phase shift accumulation in MoS_2 is highly effective and thickness variations in the order of one monolayer can be detected with a simple low-budget spectrometer assuming a spectral resolution of 3 nm, as discussed in Ref. [30] (Fig. S2).

B. Physical properties of MoS_2

Having established the relationship between optical response and thickness, we extend the fabrication of MoS_2 to standard passivated silicon wafers (50 nm SiN_x-50 nm SiO_2-Si) to better study its physical properties. Additional discussion is provided in Ref. [30]. We choose Rutherford backscattering spectroscopy (RBS), Raman spectroscopy, photoluminescence spectroscopy (PL), and x-ray diffraction (XRD) to assess the evolution of stoichiometry, crystal structure, characteristic vibrational modes, and excitonic transitions as a function of thickness and postdeposition annealing (Fig. 2). RBS is a reference-free technique that utilizes the element and depth-specific elastic backscattering of high energy particles [Fig. 2(a)] to extract compositional depth profiles [34,35]. Due to its subnanometer depth and high mass resolution, RBS is ideally suited to probe the stoichiometry, composition, and film thickness in ultrathin systems [35].

Figure 2(b) shows two representative RBS spectra corresponding to two ultrathin c-MoS_2 films. The stoichiometry and thickness of the MoS_2 layers were obtained by fitting the RBS spectra, and the best fit was achieved for a layer thickness of 1.3 ± 0.1 and 3.0 ± 0.1 nm, respectively. The measured average thickness corresponds to systems with 2 and 5 layers and agrees well with those observed in the thermochromic sensors. The spectrum of the thinnest sample ($\delta = 1.3$ nm) exhibits a small amount of argon (Ar) impurities, which is a common phenomenon observed in sputter-deposited systems [36]. According to RBS, the average S to Mo ratio is 1.7 ± 0.3 [Fig. 2(g)] corresponding to an average sulfur vacancy percentage of 15%. We attribute the formation of S vacancies to the presence of an Ar plasma during the growth process [36,37]. The presence of such vacancies can lead to the formation of gap states [37] and can significantly change the physical properties of the material [38,39].

We confirm the crystallization of the system upon isothermal annealing using x-ray diffraction (XRD). Figure 2(d) shows XRD-spectra of three selected MoS_2 films, before and after annealing at 750 K. Crystallization of MoS_2 occurs along an in-plane orientation with high nanocrystallinity and average grain size of d_{grain} of 5.5 nm [Figs. 2(c) and 2(d)]. The TEM characterization of a film with $\delta = 1.3$ nm (Fig. S5)

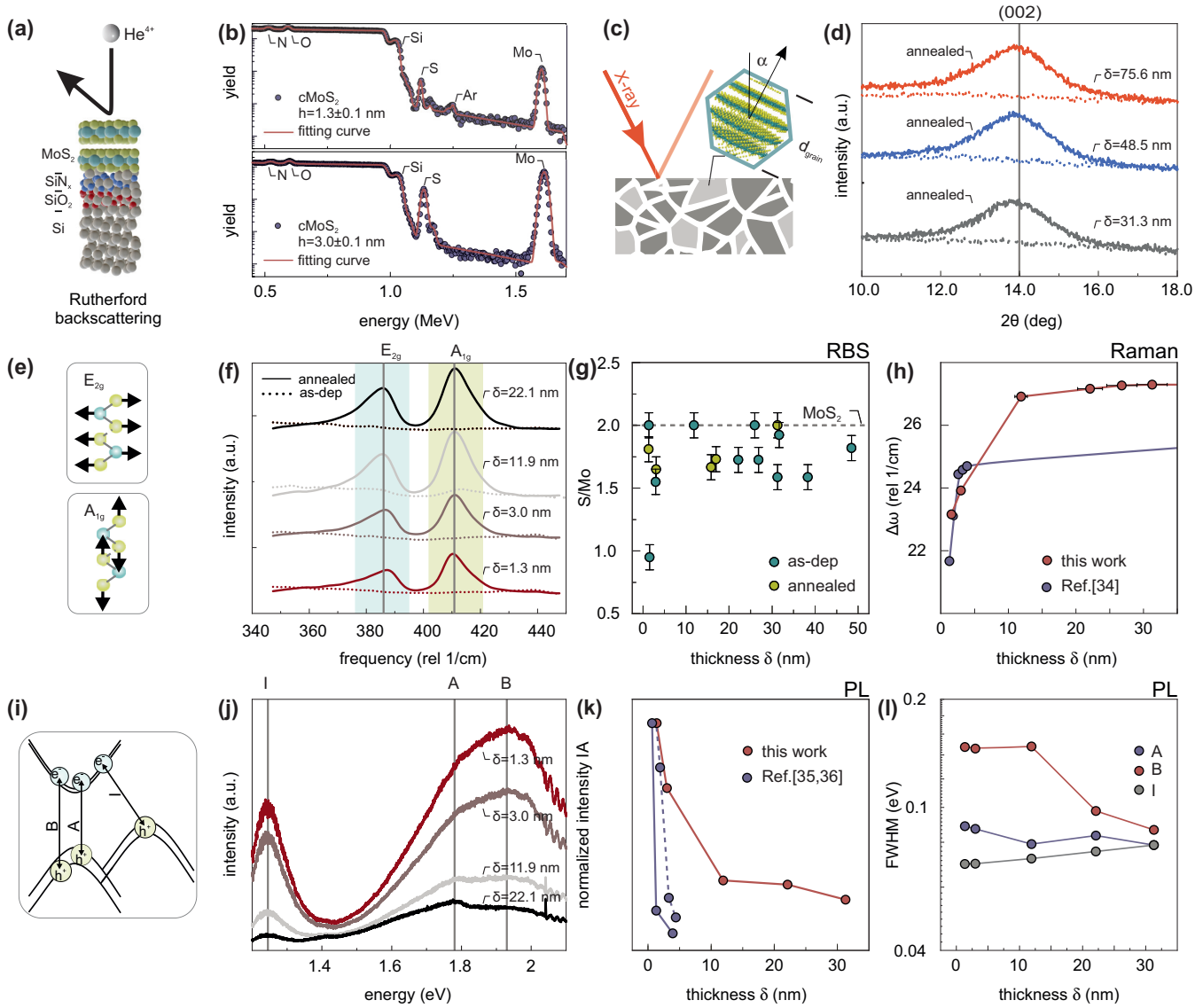

FIG. 2. (a) Schematic diagram of the backscattering process of high energy particles (2 MeV He^{4+}) on ultrathin MoS_2 on passivated silicon substrates. (b) Selected Rutherford backscattering spectra of samples with 1.3 nm (top) and 3 nm (bottom) MoS_2 on top of passivated Si wafers before annealing. The blue dots are the experimental data, while the orange line indicates the fit from which the parameters were extracted. (c) Schematic illustrating the nanocrystalline nature of the fabricated films. (d) X-ray diffraction pattern of selected thicker MoS_2 films on passivated Si both before (dashed) and after annealing (continuous). The line indicates the position of the c-MoS_2 (002) lattice plane [40]. (e) Schematic showing the characteristic vibrational modes of TMCs: E_{2g}, the in-plane vibration, and A_{1g}, the out-of-plane stretching of sulfur atoms. (f) Raman spectra of sputtered MoS_2 layers on passivated Si both before (dotted) and after annealing (solid line). (g) Mo/S ratio measured by RBS. Blue points correspond to individual as-deposited samples, while yellow points correspond to individual annealed samples. The error bar denotes the systematic error of the RBS measurement. (h) Plot of the frequency difference between the two Raman modes shown in (f) for samples with different thicknesses (red). The blue points indicate the equivalent values from the literature [41]. (i) Schematic of the A, B, and I excitonic transitions present in TMCs. (j) Photoluminescence spectra of various c-MoS_2 films on passivated Si after annealing. The lines indicate the position of the A, B, and I excitonic transitions. Peak position was determined by peak deconvolution, as shown in Fig. S6. (k) Normalized intensity of the emission of the A exciton against film thickness δ (red). The blue points indicate the equivalent values from the literature (Refs. [42,43]). (l) Full width half maximum (FWHM) of the excitonic peaks.

seems to indicate only partial crystallization. However, this could be due to the low substochiometric Mo/S ratio of the thinnest samples [Fig. 2(g)]. We refer to Ref. [30] (Table S4) for details about the crystallite size determination. The formation of such a nanocrystalline phase can lead to additional defect states, such as the accumulation of S-vacancies in the grain boundaries (GBs) [44].

To examine the combined effect of chemical and structural disorder observed by RBS and XRD on the vibrational modes of MoS_2, we turn to Raman spectroscopy. Figure 2(e) illustrates the first-order Raman modes of c-MoS_2 [41,45,46]: the out-of-plane vibration of the sulfur atoms (A_{1g}) and the in-plane vibration of Mo and S atoms (E_{2g}). The (E_{2g}) mode is an in-plane collective oscillation of Mo and S atoms, and it is

therefore susceptible to changes in stoichiometry and in-plane strain. The peaks corresponding to these modes emerge after annealing, as shown in the Raman spectra in Fig. 2(f). Both peaks exhibit asymmetrical broadening, indicating that the presence of small grain sizes induces phonon confinement effects [47]. The grain boundaries can disrupt the spatial translational symmetry, leading to a substantial reduction in phonon lifetime, ultimately resulting in an increased linewidth [Fig. 2(f)].

Although a substoichiometric Mo/S ratio has been shown to increase the frequency difference between the two Raman modes [38,39,48,49], we still observe the characteristic shift of the first-order modes as a function of thickness δ [Fig. 2(h)]. The measured frequency difference $\Delta\omega$ gets smaller in the few-layer regime. This shift indicates that, despite the high density of defects, the changes in the phononic band structure with the reduction in the number of layers is comparable to that observed for MoS_2 deposited by other techniques [25,41,50].

To extend the analysis towards the optoelectronic properties, which are also known to be thickness-dependent [42], we performed steady-state photoluminescence spectroscopy on c-MoS_2. Inspection of the obtained PL spectra [Fig. 2(j)] reveals three excitonic emission peaks, which can be attributed to indirect-gap luminescence (peak I 1.24 eV) and direct-gap hot luminescence (peak A 1.78 eV, peak B 1.93 eV), as illustrated in Fig. 2(i) [10,51]. In case the MoS_2 thickness exceeding one monolayer, the direct-gap transition occurs due to hot carriers that transiently occupy spin-orbit split valence bands near the K points [10]. It is to be noted that in addition to direct-gap hot luminescence demonstrated here, contributions of directly thermalized carriers from the fundamental band gap cannot be fully ruled out and have to be considered to contribute to the radiative excitonic emission.

The linewidths of the A and B excitons are significantly broadened, so that the two peaks cannot be distinguished without peak deconvolution (see Ref. [30], Fig. S6, and Table S3). As the linewidth of the PL signal is inversely correlated with the excitonic lifetime τ [52–54], it is a clear indicator of non-radiative recombination due to S vacancies or structural disorder [55–57]. The short excitonic lifetime makes sputtered MoS_2 films strong candidates for valleytronics [55]. The high measured B/A peak ratio [Fig. 2(k)] and the increasing linewidth of the B-exciton with decreasing film thickness [Fig. 2(l)] [55] further indicate increase defects in thinner films [55,58,59]. The intensity of direct-gap excitons A and B scales inversely with the film thickness δ [Fig. 2(k)], reminiscent of exfoliated systems [42]. This can be attributed to the direct-to-indirect band gap transition and/or to an increased defect density [56,57]. The persistence of the emissivity of these direct-gap excitons in films with thicknesses of tens of nanometers contrasts with MoS_2 fabricated through other methods. One explanation of such persistent emissivity can be traced back to the high nanocrystallinity of the system. Here, both the finite size of the crystallites of 5.5 nm and the grain boundaries have to be considered. Grain boundaries can be concieved as amorphized zones with differing dielectric constant able to critically change the dielectric screening and enhance the quantum yield of the A and B transition [60].

It is remarkable that, despite this nanocrystallinity and the sub-stoichiometry in our films, we still observe the same trends in the scaling of the electronic and phononic bandstructure with thickness as in MoS_2 obtained by other methods such as CVD or exfoliation. The notion that the physical properties prevail over their thickness dependence despite the high-defect concentration, highlights the robustness of sputtered MoS_2 films.

C. Amorphous-crystalline transition

So far, we limited the analysis of the functional properties to a mere comparison of one amorphous and one crystalline state. An interesting question is can one use the direct optical feedback to track the change of functional properties across the amorphous-crystalline transition. Such an approach can allow for valuable insights, including the determination of the crystallization temperature T_c and identification of metastable intermediates [61,62].

Figure 3(a) shows near-normal incidence reflectance spectra of three MoS_2 thin films with $\delta = 31.1$, 48.5, and 75.6 nm sputtered on SiN_x-SiO_2-Si substrates and annealed at different temperatures. All spectra exhibit a characteristic minimum in reflectance which shifts upon annealing due to the change in the optical properties of MoS_2. The inversion of the wavelength shift in Fig. 3(a) is due to the refractive index of the passivated silicon wafers being higher than that of MoS_2 for the $\delta = 31.1$ nm film minimum and being lower for the other two systems. Figure 3(b) illustrates the absolute value of the normalized relationship between $\lambda_{\min}$ and the thickness of the film. We observe a typical steplike function indicative of a first-order transition, with the average transition temperature $T_c = 499 \pm 99$ K. It should be noted that 750 K is the temperature at which the samples in Figs. 1 and 2 were annealed and that the XRD results shown in Fig. 2(b) correspond to the same batch of samples. Therefore, we attribute this shift in the minimal reflectance to crystallization and show that, for thicker films, the change in the optical properties of MoS_2 upon crystallization can be sensed without a metallic backreflector, opening the door to characterize the electrical properties of MoS_2.

We evaluated the electrical properties of our films using a four-point linear probe, as illustrated in Fig. 3(c). In Fig. 3(d), the ohmic current-voltage characteristic of the $\delta = 48.5$ nm film is depicted, illustrating an increase in sheet resistance with varying annealing temperatures, with a noticeable increase marked by the dashed line upon crystallization. The increase in sheet resistance was similarly observed for the other two film thicknesses, as depicted in Fig. 3(e). The average fitted transition temperature ($T_c = 478 \pm 93$ K) is in good agreement with the transition temperature found through the characterization of the optical properties (Table S5). An increase in sheet resistance of almost one order of magnitude upon annealing could be measured for film thicknesses down to 11.9 nm, as shown in Fig. S7. Consistent with existing research [63], we attribute this stark increase in sheet resistance upon crystalization to changes in the coordination of molybdenum atoms. The metallic homopolar Mo-Mo bonds in the amorphous state are replaced by less conductive Mo-S covalent bonds upon crystalization [22,63].

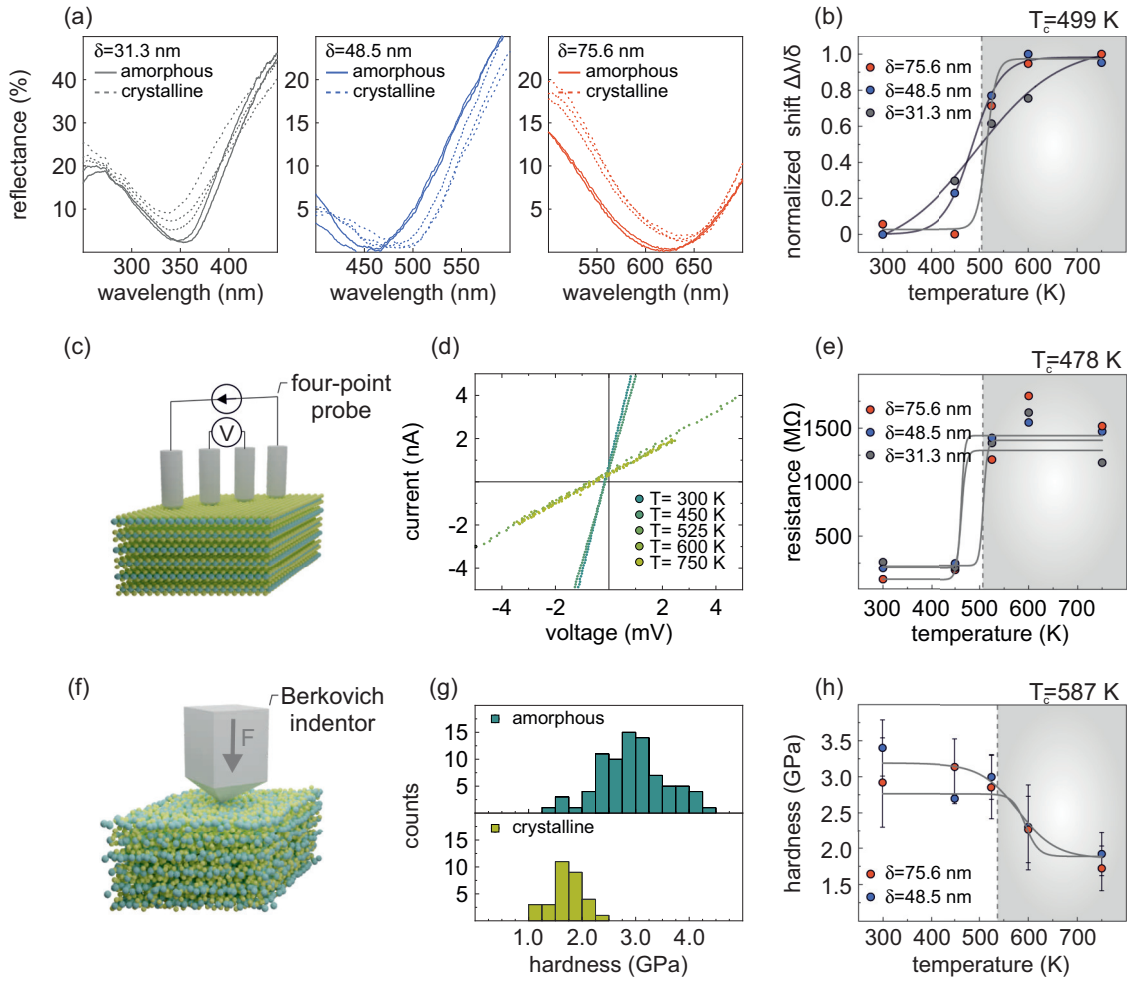

FIG. 3. (a) Near-normal incidence reflectance spectra of three selected MoS_2 systems with characteristic dip in reflection. The solid lines show the spectra of the amorphous state and the dotted lines show the reflectance spectra of the samples annealed at 450, 525, 600, and 750 K. The spacing of the dots increases with the annealing temperature. (b) Change of the minimal reflectance extracted from (a) given by $\Delta\lambda/\delta$ at different annealing temperatures. The grey shaded area indicates the region above the calculated crystallization temperature T_c. All curves exhibit a stepwise transition around T_c as fitted using a modified hyperbolic function for each MoS_2 thickness.(c) Schematic of the four-point probe used to measure the sheet resistance. (d) Current-voltage curves as measured by a four-point probe for the different crystallization states of the 48.5 nm film. (e) Evolution of the sheet resistance of selected MoS_2 systems across the amorphous-crystalline phase transition. The grey area indicates the average T_c, as fitted using a modified hyperbolic function for each MoS_2 thickness. (f) Schematic of the nanoindentation setup used to measure hardness. (g) Histograms showing the distribution of the measured hardnesses for the $\delta = 48.5$ nm film. The blue histogram at the top is for the as-deposited state, while the red histogram below was measured on the same sample annealed to 750 K. (h) Hardness of the samples annealed at different temperatures. The grey area indicates the average T_c, as fitted using a modified hyperbolic function for each MoS_2 thickness.

To characterize the mechanical properties of our films, we performed nanoindentation experiments, as illustrated by the schematic in Fig. 3(f). We observe a decrease in the hardness of the films after annealing, as shown in Figs. 3(g) and 3(h). This behavior can also be explained through the amorphous-crystalline phase transition in the film. Intramolecular bonds dominate the atomic structure of a-MoS_2 and typically lead to brittle behavior and high hardness [64]. On the contrary, the stacked structure of c-MoS_2 is characterized by strong covalent in-plane forces and weak interlayer van der Waals interactions. These interplane van der Waals interactions provide low resistance to applied forces, enabling the sliding or shearing of layers at substantially lower stress than for intramolecular bonds [65]. Interestingly, interlayer sliding also enables the superior lubrication of MoS_2 [7,65]. Therefore, during hardness measurements, the weak out-of-plane bonding in these stacked sheet structures reduces the hardness of the material by lowering the stress required for deformation and reaccommodation within the structure.

Furthermore, we observed a large peak broadening in the XRD measurements that indicates substantial out-of-plane rotations between the crystalline MoS_2 grains and the substrate [schematically illustrated in Fig. 2(c)]. These grain rotations make interlayer sliding even more accessible as a deformation mechanism under indentation loading and would further support the mechanical availability of interplane sliding. Thus, in the presence of a nanocrystalline phase, we expect a clear decrease in hardness as compared to the amorphous phase. The

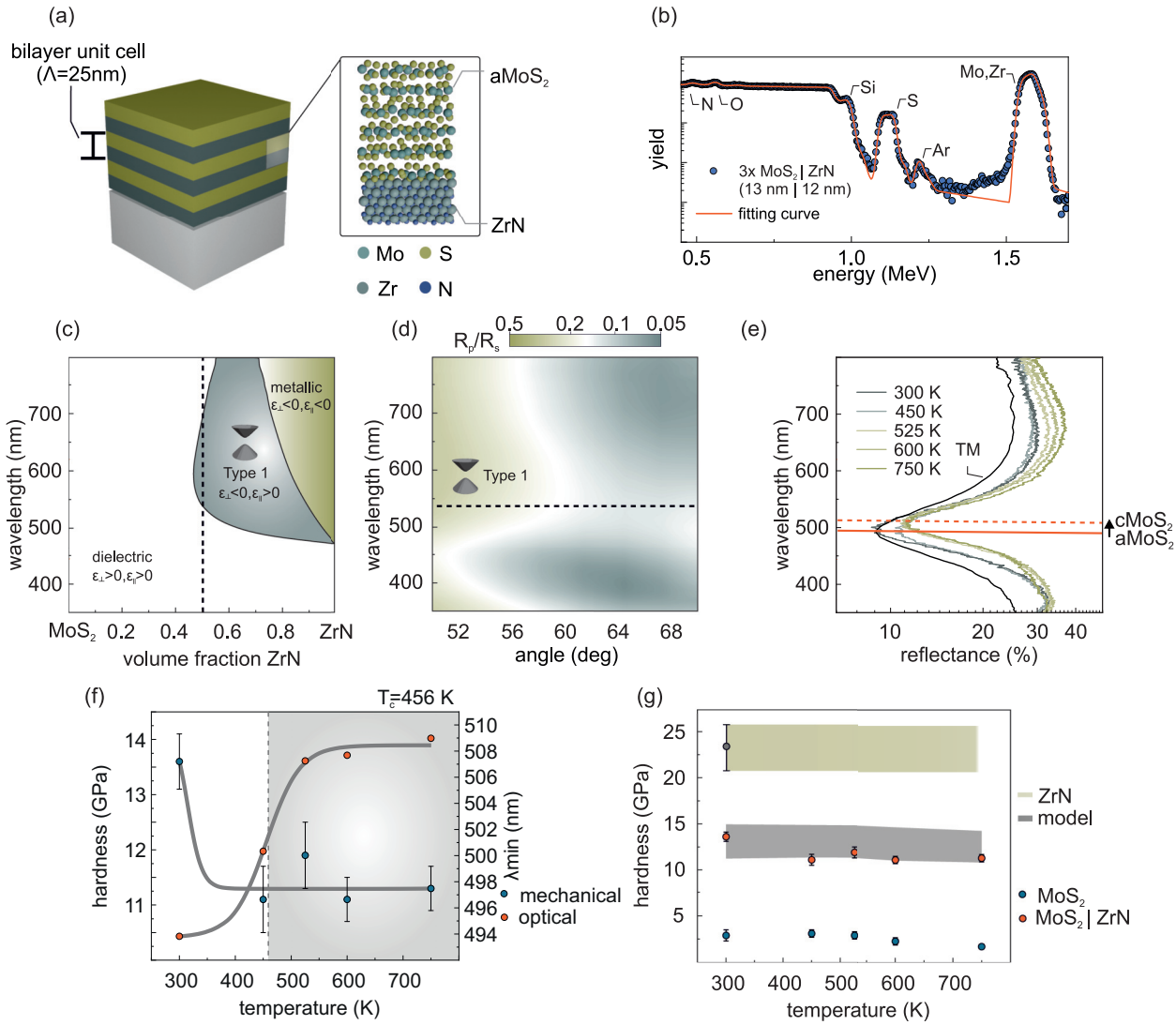

FIG. 4. (a) Schematic of the deposited ZrN-MoS_2 multilayer. (b) Rutherford backscattering spectra of the ZrN-MoS_2 multilayer. The blue dots correspond to the experimental data, while the orange line indicates the simulated spectrum. (c) Optical phase diagram for MoS_2-ZrN HMMs. The color code depicts the different zones: effective dielectric ($\epsilon_\perp > 0, \epsilon_\parallel > 0$), effective metal ($\epsilon_\perp < 0, \epsilon_\parallel < 0$), and Type I HMM ($\epsilon_\perp < 0, \epsilon_\parallel > 0$). The dashed vertical lines illustrate the measured composition. (d) Color mapping of the measured ratio in reflectance between the p- and s-polarization. The dashed line indicates the wavelength at which the transition between a dielectric and an HMM is expected. (e) Near-normal incidence reflectance spectra of the HMMs annealed at different temperatures. The dashed dark line indicates the calculated reflectance using the TM method. The horizontal red lines indicate the wavelength of the HMMs with amorphous (solid) and crystalline (dashed) MoS_2, respectively. (f) Change in the hardness (blue) and wavelength of the reflected minimum (red) of the multilayer metamaterial with the temperature of annealing. The grey area indicates the temperatures after which c-MoS_2 is expected, as fitted from the optical data with a modified hyperbolic function. (g) Hardness of the multilayer metamaterial (red) and MoS_2 thin film (blue) annealed at different temperatures. The semi-transparent yellow area shows the measured hardness of ZrN. The semitransparent grey area indicates the expected results calculated using the rule of mixtures.

calculated crystallization temperature ($T_c = 587 \pm 106$ K) is higher than the one found through electrical and optical characterization but falls within the error range.

D. Few-layer MoS_2 multilayer composites

The ability to rapidly track the thickness and phase of sputter-deposited MoS_2 opens the possibility of creating more complex stacked photonic systems combining MoS_2 with non-van der Waals materials. We illustrate this by fabricating a MoS_2|ZrN hyperbolic metamaterial [66,67]. These architected materials enable the engineering of the local density of optical states (LDOS), enhancement of spontaneous emission, and confinement of light to small modal volumes [67]. Furthermore, hyperbolic metamaterials are considered as a promising platform to create plexcitons, strongly coupled plasmon-excitonic quasiparticles [68,69].

Figure 4(a) illustrates the metamaterial design consisting of alternating layers of ZrN and MoS_2. The bilayer unit cell

Λ and the volume fraction ϕ were chosen to be 25 nm and 0.5, respectively. The composition and thickness profile of our fabricated ZrN-MoS_2 HMM was measured by RBS and is shown in Fig. 4(b). Due to the small energy separation between Mo and Zr, the alternation of the layers is only resolvable within the simulation of the spectrum.

According to effective medium theory, the chosen metamaterial design exhibits an optical topological transition (OTT) in the visible spectrum [Fig. 4(c)] [66,70]. Due to the emergence of new optical states, the isofrequency surface of the HMM changes its shape from a sphere (dielectric phase) to a hyperbole (type 1 phase). We experimentally observe this transition between the two topologies by measuring the R_p/R_s ratio [Fig. 4(d)], since the propagation of hyperbolic modes is limited to *p*-polarized light [71]. The transition from the dielectric phase to the Type I HMM phase is due to a change of sign in the out-of-plane permittivity $\epsilon_\perp$ and results in a discontinuity in the pseudo-Brewster angle ([71,72]). Our measurements replicate this discontinuity at $\lambda = 525$ nm, as shown in Fig. 4(d).

When annealed across the amorphous-crystalline transition, the optical properties of the HMMs change. Figure 4(e) compares the measured reflectance at normal incidence of HMMs annealed at different temperatures. All HMMs exhibit a Lorentz-like dip in reflectance which is caused by coupling to propagating modes with high-k wave vector. The reflectance minimum redshifts upon annealing [Fig. 4(f)], and the shift reproduces the characteristic profile of the phase transition as observed in Fig. 3.

Understanding the composite's architecture also enables the design of the multilayer's mechanical properties. We observe that the hardness of the MoS_2-ZrN multilayer decreases upon annealing, following the same trend as the hardness of MoS_2. The mechanical properties of MoS_2 can be deconvoluted using the rule of mixtures, as illustrated in Fig. 4(g). The hardness value of ZrN is taken as the mean hardness measured in the as-deposited samples, while the value for H_{MoS_2} comes from the hardness measurements shown in Fig. 3(h). At 0.5 volume fraction ϕ, the calculated hardness for the as-deposited samples is in good agreement with the measured hardness. Thus the composite mechanical response of the HMM does not indicate strong size effect contributions arising from the ultrathin layers. Additionally, mechanical degradation in ZrN after annealing could contribute to a reduction in multilayer hardness that is not reflected in the calculated values. Another possible contributing factor could include the relative fraction of probed materials [73]. As c-MoS_2 is softer than a-MoS_2, it will have a larger plastic zone and therefore a larger contributing volume to the probed material under indentation conditions. This would increase the relative volume fraction of MoS_2 and thus reduce the predicted hardness.

The results demonstrate that the rule of mixtures can be used to design the hardness of layered metamaterials, in a similar fashion to how the effective medium approximation can be used to design the optical phase diagram of the multilayer, opening the door to the design of hyperbolic metamaterials with tailored mechanical properties. With an order of magnitude difference in hardness between the constituents, MoS_2-ZrN multilayers provide a large space to tailor the mechanical response to the distinct hardnesses. Remarkably, the applicability of the rule of mixtures allows for rapid prototyping and design in comparison to first-principle methods [74].

The multilayer can also be used to determine the hardness of MoS_2 $\delta = 13$ nm ($\sim$20 monolayers) in a deconvoluted manner. In addition to enabling sensing the amorphous-crystalline phase transition and displaying hyperbolic optical modes in the visible, the ZrN-MoS_2 multilayer shows the characteristic MoS_2 photoluminesce response, as shown in Fig. S8 in Ref. [30]. These stacked designs pave the way for the realization of plexitonic devices with tailored mechanical properties, enabling the study of the effect of strain in the exciton-plasmonic quasiparticles, among others.

IV. CONCLUSION

The present work highlights the potential of smart sensing to determine the phase, thickness, and functional properties of MoS_2 fabricated by bottom-up magnetron sputtering. The sensors can detect MoS_2 thickness variations down to one monolayer and display a full gamut of colors obtained by exploiting the freedom in substrate choice and control over thickness and phase. The coloration can be used as a fast postdeposition feedback mechanism, opening the door to further controlling the thickness and crystallinity through MoS_2 fabrication.

We show that the effects of the phase change upon crystallization are crucial for understanding the phononic and electronic band structures of our films. For example, we observe that even in bulklike samples, the direct-gap hot luminescence typically associated with monolayer MoS_2 dominates the PL spectra. We link the unexpected enhancement in quantum yield to nanocrystallinity and related finite size effects on the excitonic emission. Despite the defects induced by our fabrication technique, the electronic and phononic band structures of our films shift with thickness in a way similar to MoS_2 produced by exfoliation or CVD.

Leveraging the changes in optical properties through crystallization, we explore the accompanying changes in electrical and mechanical properties of MoS_2 through the phase transition. We further demonstrate that the valuable insights from this optical sensing can be garnered to fabricate an MoS_2-based HMM that allowed us to detect changes in the hardness of few-layer MoS_2 with a simple low-budget spectrometer. The hardness of these multilayers can be approximated with the rule of mixtures, opening the door to the rapid design of hyperbolic metamaterials with tailored mechanical properties. Additionally, the demonstrated presence of excitonic features in the MoS_2-based multilayers paves the way for the study of interesting physical phenomena such as the effect of strain plexitonic modes.

Our findings provide insights into the functional properties of amorphous and crystalline MoS_2 across different thicknesses and show a viable route towards versatile wafer-scale fabrication of MoS_2 thin films and MoS_2-based architectures, thus contributing to the development of MoS_2-based devices.

ACKNOWLEDGMENTS

The authors acknowledge the infrastructure and support of FIRST and ScopeM. The authors acknowledge the valuable help from Y. Chen, J. Sendra, C. Lauener, H. Kuang, and A. Korde; and the discussions with J. Wohlwend, R. Kaindl, and F. Krogh. J.L.O.-P. thanks for the financial support from the ETH research grant (ETH-47 18-1).

[1] B. Lojek, *History of Semiconductor Engineering* (Springer, Berlin, Heidelberg, 2007).

[2] S. Wang, X. Liu, and P. Zhou, The road for 2D semiconductors in the silicon age, Adv. Mater. **34**, 2106886 (2022).

[3] D. Gupta, V. Chauhan, and R. Kumar, A comprehensive review on synthesis and applications of molybdenum disulfide (MoS_2) material: Past and recent developments, Inorg. Chem. Commun. **121**, 108200 (2020).

[4] J. P. Wilcoxon, G. Samara, and P. Newcomer, Optical features of nanosize iron and molybdenum sulfide clusters, MRS Online Proc. Libr. **358**, 277 (1994).

[5] K. M. Kadiev, A. M. Gyul'maliev, and M. K. Kadieva, On the mechanism of sulfur removal during hydroconversion in the presence of a catalyst MoS_2, Russ. J. Appl. Chem. **94**, 518 (2021).

[6] T. Spalvins and Lewis Research Center, *Bearing Endurance Tests in Vacuum for Sputtered Molybdenum Disulfide Films* (National Aeronautics and Space Administration, Washington, DC, 1975), Vol. NASA TM X-3193.

[7] L. Rapoport, A. Moshkovich, V. Perfilyev, I. Lapsker, G. Halperin, Y. Itovich, and I. Etsion, Friction and wear of MoS_2 films on laser textured steel surfaces, Surf. Coat. Technol. **202**, 3332 (2008).

[8] O. V. Yazyev and A. Kis, MoS_2 and semiconductors in the flatland, Mater. Today **18**, 20 (2015).

[9] K. F. Mak, M. Y. Sfeir, J. A. Misewich, and T. F. Heinz, The evolution of electronic structure in few-layer graphene revealed by optical spectroscopy, Proc. Natl. Acad. Sci. USA **107**, 14999 (2010).

[10] K. F. Mak, C. Lee, J. Hone, J. Shan, and T. F. Heinz, Atomically thin MoS_2: A new direct-gap semiconductor, Phys. Rev. Lett. **105**, 136805 (2010).

[11] S.-G. Kim, S.-H. Kim, J. Park, G.-S. Kim, J.-H. Park, K. C. Saraswat, J. Kim, and H.-Y. Yu, Infrared detectable MoS_2 phototransistor and its application to artificial multilevel optic-neural synapse, ACS Nano **13**, 10294 (2019).

[12] A. Di Bartolomeo, A. Kumar, O. Durante, A. Sessa, E. Faella, L. Viscardi, K. Intonti, F. Giubileo, N. Martucciello, P. Romano, S. Sleziona, and M. Schleberger, Temperature-dependent photoconductivity in two-dimensional MoS_2 transistors, Mater. Today Nano **24**, 100382 (2023).

[13] S. Hwangbo, L. Hu, A. T. Hoang, J. Y. Choi, and J.-H. Ahn, Wafer-scale monolithic integration of full-colour micro-LED display using MoS_2 transistor, Nat. Nanotechnol. **17**, 500 (2022).

[14] A. D. Al-Ghiffari, N. A. Ludin, M. L. Davies, R. M. Yunus, and M. S. Suait, Systematic review of molybdenum disulfide for solar cell applications: Properties, mechanism and application, Mater. Today Commun. **32**, 104078 (2022).

[15] K. F. Mak, D. Xiao, and J. Shan, Light-valley interactions in 2D semiconductors, Nat. Photon. **12**, 451 (2018).

[16] J. Zhang, L. Du, S. Feng, R.-W. Zhang, B. Cao, C. Zou, Y. Chen, M. Liao, B. Zhang, S. A. Yang, G. Zhang, and T. Yu, Enhancing and controlling valley magnetic response in MoS_2/WS_2 heterostructures by all-optical route, Nat. Commun. **10**, 4226 (2019).

[17] E. C. Ahn, 2D materials for spintronic devices, npj 2D Mater. Appl. **4**, 17 (2020).

[18] M.-C. Chang, P.-H. Ho, M.-F. Tseng, F.-Y. Lin, C.-H. Hou, I.-K. Lin, H. Wang, P.-P. Huang, C.-H. Chiang, Y.-C. Yang, I.-T. Wang, H.-Y. Du, C.-Y. Wen, J.-J. Shyue, C.-W. Chen, K.-H. Chen, P.-W. Chiu, and L.-C. Chen, Fast growth of large-grain and continuous MoS_2 films through a self-capping vapor-liquid-solid method, Nat. Commun. **11**, 3682 (2020).

[19] A. Quellmalz, X. Wang, S. Sawallich, B. Uzlu, M. Otto, S. Wagner, Z. Wang, M. Prechtl, O. Hartwig, S. Luo, G. S. Duesberg, M. C. Lemme, K. B. Gylfason, N. Roxhed, G. Stemme, and F. Niklaus, Large-area integration of two-dimensional materials and their heterostructures by wafer bonding, Nat. Commun. **12**, 917 (2021).

[20] M. Timpel, G. Ligorio, A. Ghiami, L. Gavioli, E. Cavaliere, A. Chiappini, F. Rossi, L. Pasquali, F. Gärisch, E. J. W. List-Kratochvil, P. Nozar, A. Quaranta, R. Verucchi, and M. V. Nardi, 2D-MoS_2 goes 3D: transferring optoelectronic properties of 2D MoS_2 to a large-area thin film, npj 2D Mater. Appl. **5**, 64 (2021).

[21] P. Cao, J. Peng, S. Liu, Y. Cui, Y. Hu, B. Chen, J. Li, and M. Zhai, Tuning the composition and structure of amorphous molybdenum sulfide/carbon black nanocomposites by radiation technique for highly efficient hydrogen evolution, Sci. Rep. **7**, 16048 (2017).

[22] M. Krbal, V. Prokop, A. A. Kononov, J. R. Pereira, J. Mistrik, A. V. Kolobov, P. J. Fons, Y. Saito, S. Hatayama, Y. Shuang, Y. Sutou, S. A. Rozhkov, J. R. Stellhorn, S. Hayakawa, I. Pis, and F. Bondino, Amorphous-to-Crystal transition in quasi-two-dimensional MoS_2: Implications for 2D electronic devices, ACS Appl. Nano Mater. **4**, 8834 (2021).

[23] Z. Huang, T. Zhang, J. Liu, L. Zhang, Y. Jin, J. Wang, K. Jiang, S. Fan, and Q. Li, Amorphous MoS_2 photodetector with ultra-broadband response, ACS Appl. Electron. Mater. **1**, 1314 (2019).

[24] L. Wu, A. Longo, N. Y. Dzade, A. Sharma, M. M. R. M. Hendrix, A. A. Bol, N. H. de Leeuw, E. J. M. Hensen, and J. P. Hofmann, The origin of high activity of amorphous MoS_2 in the hydrogen evolution reaction, ChemSusChem **12**, 4383 (2019).

[25] J. Tao, J. Chai, X. Lu, L. M. Wong, T. I. Wong, J. Pan, Q. Xiong, D. Chi, and S. Wang, Growth of wafer-scale MoS_2 monolayer by magnetron sputtering, Nanoscale **7**, 2497 (2015).

[26] T. F. Babuska, J. F. Curry, M. T. Dugger, M. R. Jones, F. W. DelRio, P. Lu, Y. Xin, T. Grejtak, R. Chrostowski, F. Mangolini, N. C. Strandwitz, M. I. Chowdhury, G. L. Doll, and B. A. Krick, Quality control metrics to assess MoS_2 sputtered films for tribological applications, Tribol. Lett. **70**, 103 (2022).

[27] M. A. Kats, R. Blanchard, P. Genevet, and F. Capasso, Nanometre optical coatings based on strong interference effects in highly absorbing media, Nat. Mater. **12**, 20 (2013).

[28] K. M. Islam, R. Synowicki, T. Ismael, I. Oguntoye, N. Grinalds, and M. D. Escarra, In-plane and out-of-plane optical properties of monolayer, few-layer, and thin-film MoS_2 from 190 to 1700 nm and their application in photonic device design, Adv. Photonics Res. **2**, 2000180 (2021).

[29] X. Yin, Q. Wang, L. Cao, C. S. Tang, X. Luo, Y. Zheng, L. M. Wong, S. J. Wang, S. Y. Quek, W. Zhang, A. Rusydi, and A. T. S. Wee, Tunable inverted gap in monolayer quasi-metallic MoS_2 induced by strong charge-lattice coupling, Nat. Commun. **8**, 486 (2017).

[30] See Supplemental Material at http://link.aps.org/supplemental/10.1103/PhysRevB.110.115303 for contains technical details related to the fabrication and experimental characterization presented in the main text, that are not essential to the understanding of the arguments developed there, which includes Refs. [28,75–86].

[31] P. Markoš and C. Soukoulis, *Wave Propagation. From Electrons to Photonic Crystals and Left-Handed Materials* (Princeton University Press, Princeton, 2008).

[32] S. J. Byrnes, Multilayer optical calculations, arXiv:1603.02720.

[33] M. A. Kats and F. Capasso, Optical absorbers based on strong interference in ultrathin films, Laser Photon. Rev. **10**, 735 (2016).

[34] H. Galinski, T. Ryll, L. Schlagenhauf, F. Rechberger, S. Ying, L. J. Gauckler, F. C. F. Mornaghini, Y. Ries, R. Spolenak, and M. Döbeli, Dealloying of platinum-aluminum thin films: Dynamics of pattern formation, Phys. Rev. Lett. **107**, 225503 (2011).

[35] Y. Wang and M. Nastasi, *Handbook of Modern Ion Beam Materials Analysis* (MRS, Materials Research Soc., 2010).

[36] D. Gupta, V. Chauhan, and R. Kumar, Sputter deposition of 2D MoS_2 thin films -A critical review from a surface and structural perspective, Inorg. Chem. Commun. **144**, 109848 (2022).

[37] H. Li, C. Tsai, A. L. Koh, L. Cai, A. W. Contryman, A. H. Fragapane, J. Zhao, H. S. Han, H. C. Manoharan, F. Abild-Pedersen, J. K. Nørskov, and X. Zheng, Activating and optimizing MoS_2 basal planes for hydrogen evolution through the formation of strained sulphur vacancies, Nat. Mater. **15**, 48 (2016).

[38] O. Alev and E. Goldenberg, Nanostructured MoS_2 thin films: Effect of substrate temperature on microstructure, optical, and electrical properties, J. Vac. Sci. Technol. **41**, 033408 (2023).

[39] M. Donarelli, F. Bisti, F. Perrozzi, and L. Ottaviano, Tunable sulfur desorption in exfoliated MoS_2 by means of thermal annealing in ultra-high vacuum, Chem. Phys. Lett. **588**, 198 (2013).

[40] V. Buck, Structure and density of sputtered MoS_2-films, Vacuum **36**, 89 (1986).

[41] C. Lee, H. Yan, L. E. Brus, T. F. Heinz, J. Hone, and S. Ryu, Anomalous lattice vibrations of single- and few-layer MoS_2, ACS Nano **4**, 2695 (2010).

[42] A. Splendiani, L. Sun, Y. Zhang, T. Li, J. Kim, C.-Y. Chim, G. Galli, and F. Wang, Emerging photoluminescence in monolayer MoS_2, Nano Lett. **10**, 1271 (2010).

[43] G. Eda, H. Yamaguchi, D. Voiry, T. Fujita, M. Chen, and M. Chhowalla, Photoluminescence from chemically exfoliated MoS_2, Nano Lett. **11**, 5111 (2011).

[44] V. K. Sangwan, D. Jariwala, I. S. Kim, K.-S. Chen, T. J. Marks, L. J. Lauhon, and M. C. Hersam, Gate-tunable memristive phenomena mediated by grain boundaries in single-layer MoS_2, Nat. Nanotechnol. **10**, 403 (2015).

[45] K.-G. Zhou, F. Withers, Y. Cao, S. Hu, G. Yu, and C. Casiraghi, Raman modes of MoS_2 used as fingerprint of van der Waals interactions in 2-D crystal-based heterostructures, ACS Nano **8**, 9914 (2014).

[46] H. J. Conley, B. Wang, J. I. Ziegler, R. F. Haglund Jr., S. T. Pantelides, and K. I. Bolotin, Bandgap engineering of strained monolayer and bilayer MoS_2, Nano Lett. **13**, 3626 (2013).

[47] S. Mignuzzi, A. J. Pollard, N. Bonini, B. Brennan, I. S. Gilmore, M. A. Pimenta, D. Richards, and D. Roy, Effect of disorder on raman scattering of single-layer Mos_2, Phys. Rev. B **91**, 195411 (2015).

[48] W. M. Parkin, A. Balan, L. Liang, P. M. Das, M. Lamparski, C. H. Naylor, J. A. Rodríguez-Manzo, A. T. C. Johnson, V. Meunier, and M. Drndić, Raman shifts in electron-irradiated monolayer MoS_2, ACS Nano **10**, 4134 (2016).

[49] H.-J. Kim, D. Kim, S. Jung, M.-H. Bae, Y. J. Yun, S. N. Yi, J.-S. Yu, J.-H. Kim, and D. H. Ha, Changes in the Raman spectra of monolayer MoS_2 upon thermal annealing, J. Raman Spectrosc. **49**, 1938 (2018).

[50] A. Mazaheri, M. Lee, H. S. J. van der Zant, R. Frisenda, and A. Castellanos-Gomez, MoS_2-on-paper optoelectronics: drawing photodetectors with van der Waals semiconductors beyond graphite, Nanoscale **12**, 19068 (2020).

[51] A. Leonhardt, C. J. L. de la Rosa, T. Nuytten, L. Banszerus, S. Sergeant, V. K. Mootheri, T. Taniguchi, K. Watanabe, C. Stampfer, C. Huyghebaert, and S. De Gendt, Use of the indirect photoluminescence peak as an optical probe of interface defectivity in MoS_2, Adv. Mater. Interfaces **7**, 2000413 (2020).

[52] O. A. Ajayi, J. V. Ardelean, G. D. Shepard, J. Wang, A. Antony, T. Taniguchi, K. Watanabe, T. F. Heinz, S. Strauf, X.-Y. Zhu, and J. C. Hone, Approaching the intrinsic photoluminescence linewidth in transition metal dichalcogenide monolayers, 2D Mater. **4**, 031011 (2017).

[53] M. Selig, G. Berghäuser, A. Raja, P. Nagler, C. Schüller, T. F. Heinz, T. Korn, A. Chernikov, E. Malic, and A. Knorr, Excitonic linewidth and coherence lifetime in monolayer transition metal dichalcogenides, Nat. Commun. **7**, 13279 (2016).

[54] M. Kira and S. W. Koch, Many-body correlations and excitonic effects in semiconductor spectroscopy, Prog. Quantum Electron. **30**, 155 (2006).

[55] K. M. McCreary, A. T. Hanbicki, S. V. Sivaram, and B. T. Jonker, A- and B-exciton photoluminescence intensity ratio as a measure of sample quality for transition metal dichalcogenide monolayers, APL Mater. **6**, 111106 (2018).

[56] S. Tongay, J. Suh, C. Ataca, W. Fan, A. Luce, J. S. Kang, J. Liu, C. Ko, R. Raghunathanan, J. Zhou, F. Ogletree, J. Li, J. C. Grossman, and J. Wu, Defects activated photoluminescence in two-dimensional semiconductors: interplay between bound, charged and free excitons, Sci. Rep. **3**, 2657 (2013).

[57] H. Nan, Z. Wang, W. Wang, Z. Liang, Y. Lu, Q. Chen, D. He, P. Tan, F. Miao, X. Wang, J. Wang, and Z. Ni, Strong photoluminescence enhancement of MoS_2 through defect engineering and oxygen bonding, ACS Nano **8**, 5738 (2014).

[58] R. Kaupmees, H.-P. Komsa, and J. Krustok, Photoluminescence study of B-trions in MoS_2 monolayers with high density of defects, Physica Status Solidi (B) **256**, 1800384 (2019).

[59] J. Wang, C. Huang, Y. You, Q. Guo, G. Xue, H. Hong, Q. Jiao, D. Yu, L. Du, Y. Zhao, and K. Liu, Monitoring the material quality of two-dimensional transition metal dichalcogenides, J. Phys. Chem. C **126**, 3797 (2022).

[60] Y. Lin, X. Ling, L. Yu, S. Huang, A. L. Hsu, Y.-H. Lee, J. Kong, M. S. Dresselhaus, and T. Palacios, Dielectric screening of excitons and trions in single-layer MoS_2, Nano Lett. **14**, 5569 (2014).

[61] A. V. Kolobov, Y. Saito, P. Fons, and M. Krbal, Structural metastability in chalcogenide semiconductors: The role of chemical bonding, Phys. Status Solidi (B) **257**, 2000138 (2020).

[62] D. A. Kitchaev and G. Ceder, Evaluating structure selection in the hydrothermal growth of FeS_2 pyrite and marcasite, Nat. Commun. **7**, 13799 (2016).

[63] M. Krbal, J. Prikryl, I. Pis, V. Prokop, J. Rodriguez Pereira, and A. V. Kolobov, Anomalous electrical conductivity change in MoS_2 during the transition from the amorphous to crystalline phase, Ceram. Int. **49**, 2619 (2023).

[64] W. Cai and W. D. Nix, *Imperfections in Crystalline Solids* (Cambridge University Press, Cambridge, 2016).

[65] P. Serles, E. Nicholson, J. Tam, N. Barri, J.-B. Chemin, G. Wang, Y. Michel, C. V. Singh, P. Choquet, A. Saulot, T. Filleter, and G. Colas, High performance space lubrication of MoS_2 with tantalum, Adv. Funct. Mater. **32**, 2110429 (2022).

[66] J. L. Ocana-Pujol, L. Forster, R. Spolenak, and H. Galinski, Strain-driven thermal and optical instability in silver/amorphous-silicon hyperbolic metamaterials, Adv. Opt. Mater. **10**, 2201749 (2022).

[67] C. L. Cortes, W. Newman, S. Molesky, and Z. Jacob, Quantum nanophotonics using hyperbolic metamaterials, J. Opt. **16**, 129501 (2014).

[68] P. Zheng, S. Semancik, and I. Barman, Quantum plexcitonic sensing, Nano Lett. **23**, 9529 (2023).

[69] Q. Zhao, W.-J. Zhou, Y.-H. Deng, Y.-Q. Zheng, Z.-H. Shi, L. K. Ang, Z.-K. Zhou, and L. Wu, Plexcitonic strong coupling: unique features, applications, and challenges, J. Phys. D **55**, 203002 (2022).

[70] H. N. S. Krishnamoorthy, Z. Jacob, E. Narimanov, I. Kretzschmar, and V. M. Menon, Topological transitions in metamaterials, Science **336**, 205 (2012).

[71] A. J. Hoffman, L. Alekseyev, S. S. Howard, K. J. Franz, D. Wasserman, V. A. Podolskiy, E. E. Narimanov, D. L. Sivco, and C. Gmachl, Negative refraction in semiconductor metamaterials, Nat. Mater. **6**, 946 (2007).

[72] H. Cho, Y. Yang, D. Lee, S. So, and J. Rho, Experimental demonstration of broadband negative refraction at visible frequencies by critical layer thickness analysis in a vertical hyperbolic metamaterial, Nanophoton. **10**, 3871 (2021).

[73] B.-W. Choi, D.-H. Seo, and J.-i. Jang, A nanoindentation study on the micromechanical characteristics of API X100 pipeline steel, Met. Mater. Int. **15**, 373 (2009).

[74] A. Calzolari, A. Catellani, M. Buongiorno Nardelli, and M. Fornari, Hyperbolic Metamaterials with extreme mechanical hardness, Adv. Opt. Mater. **9**, 2001904 (2021).

[75] N. J. Simrick, J. A. Kilner, and A. Atkinson, Thermal stability of silver thin films on zirconia substrates, Thin Solid Films **520**, 2855 (2012).

[76] S. Hieke, B. Breitbach, G. Dehm, and C. Scheu, Microstructural evolution and solid state dewetting of epitaxial Al thin films on sapphire ($\alpha - Al_2O_3$), Acta Mater. **133**, 356 (2017).

[77] A. Sharipova, L. Klinger, A. Bisht, B. B. Straumal, and E. Rabkin, Solid-state dewetting of thin Au films on oxidized surface of biomedical TiAlV alloy, Acta Mater. **231**, 117919 (2022).

[78] R. C. Sharma and Y. A. Chang, The Ag-S (Silver-Sulfur) system, Bull. Alloy Phase Diagrams **7**, 263 (1986).

[79] R. C. Sharma and Y. A. Chang, The Al-S (Aluminum-Sulfur) system, J. Phase Equilib. **8**, 128 (1987).

[80] H. Okamoto and T. B. Massalski, The Au-S (Gold-Sulfur) system, Bull. Alloy Phase Diagrams **6**, 518 (1985).

[81] L. Gribaudo, D. Arias, and J. Abriata, The N-Zr (Nitrogen-Zirconium) system, J. Phase Equilib. **15**, 441 (1994).

[82] C. G. Ribbing and A. Roos, - Zirconium Nitride (ZrN) Hafnium Nitride (HfN), in *Handbook of Optical Constants of Solids*, edited by E. D. Palik (Academic Press, Burlington, 1997), pp. 351–369.

[83] O. Hassel, VI. Über die kristallstruktur des molybdänglanzes, Z. Kristallogr. Cryst. Mater. **61**, 92 (1924).

[84] K. Constant, R. Kieffer, and P. Ettmayer, Über das pseudoternäre system "ZrO"-ZrN-ZrC, Monatshefte Chem./Chem. Mon. **106**, 823 (1975).

[85] M. L. Falk and J. Langer, Deformation and failure of amorphous, solidlike materials, Annu. Rev. Condens. Matter Phys. **2**, 353 (2011).

[86] H. F. Wang, X. Yang, H. Bangert, P. Torzicky, and L. Wen, Two-dimensional finite element method simulation of Vickers indentation of hardness measurements on TiN-coated steel, Thin Solid Films **214**, 68 (1992).